DISCLAIMER

This document was prepared as an account of work sponsored by the United States Government. While this document is believed to contain correct information, neither the United States Government nor any agency thereof, nor The Regents of the University of California, nor any of their employees, makes any warranty, express or implied, or assumes any legal responsibility for the accuracy, completeness, or usefulness of any information, apparatus, product, or process disclosed, or represents that its use would not infringe privately owned rights. Reference herein to any specific commercial product, process, or service by its trade name, trademark, manufacturer, or otherwise, does not necessarily constitute or imply its endorsement, recommendation, or favoring by the United States Government or any agency thereof, or The Regents of the University of California. The views and opinions of authors expressed herein do not necessarily state or reflect those of the United States Government or any agency thereof or The Regents of the University of California.

Atomic-Level Control of the Thermoelectric Properties in Polytypoid Nanowires

Sean C. Andrews[1,2]*, Melissa A. Fardy[1,2]*, Michael C. Moore[1,2]*, Shaul Aloni[2], Minjuan Zhang[3], Velimir Radmilovic[2,4], & Peidong Yang[1,2]

[1]Department of Chemistry, University of California, Berkeley, California 94720.

[2]Materials Science Division, Lawrence Berkeley National Laboratory, Berkeley, California 94720.

[3]Materials Research Department, Toyota Research Institute of North America, Toyota Motor Engineering & Manufacturing North America (TEMA) Inc., 1555 Woodridge Avenue, Ann Arbor, Michigan 48105

[4]National Center for Electron Microscopy, Lawrence Berkeley National Laboratory, Berkeley, California 94720.

*These authors contributed equally to this work.

Abstract

Thermoelectric materials have generated interest as a means of increasing the efficiency of power generation through the scavenging of waste heat. Materials containing nanometer-sized structural and compositional features can exhibit enhanced thermoelectric performance due to the decoupling of certain electrical and thermal properties, but the extent to which these features can be controlled is often limited. Here we report a simple synthesis of $M_2O_3(ZnO)_n$ (M = In, Ga, Fe) nanowires with controllable polytypoid structures, where the nanostructured features are tuned by adjusting the amount of metal precursor. Single-nanowire thermal and electrical measurements on $In_{2-x}Ga_xO_3(ZnO)_n$ reveal a simultaneous improvement in all contributing factors to the thermoelectric figure of merit, giving an order of magnitude enhancement over similar bulk materials at room temperature.

Introduction

The increasing environmental concerns associated with fossil fuel-based energy production have induced a wave of scientific research into affordable alternative energy sources that are both clean and renewable (*1*). While efforts into green power generation continue in a variety of exciting and promising directions, one avenue that has caught the attention of the scientific community over the past few years is thermoelectrics, wherein electrical power is generated through the scavenging of waste heat. The efficiency of this conversion is related to the material-dependent figure of merit, $zT=S^2\sigma T/k$, where S, σ, T, and k represent the Seebeck coefficient, electrical conductivity, absolute temperature, and thermal conductivity, respectively. Though this has been a topic of scientific study for a number of decades, material engineering directed at maximizing zT has been complicated by several interdependencies of the previously mentioned parameters, limiting the efficiency (*2*). Specifically, the Seebeck coefficient's inverse dependence on carrier concentration is at odds with its direct effect on the electrical conductivity. An additional problem is that electrons carry both charge and heat, causing a synchronous increase in the electrical and thermal conductivities. While the interplay of these parameters have limited zT of bulk materials to ~1 at 300 K, theoretical studies pioneered by Hicks and Dresselhaus predict that it is possible to increase zT by using low dimensional materials, for example, nanowires (*3*). The enhancement can be attributed to two factors: electronic band structure changes caused by quantum confinement (increasing the Seebeck coefficient) and enhanced interface phonon scattering (reducing the lattice thermal conductivity) (*4, 5, 6*). Experimentally, both enhancements have been shown separately in certain nanostructured materials (*7, 8, 9, 10, 11, 12, 13*).

Superlattices contain periodic compositional and structural features, typically on the nanometer scale (*14*), making them promising candidates for thermoelectric applications. Early work discovered that $M_2O_3(ZnO)_n$ superlattice structures arise when ZnO is alloyed with high amounts of In, forming layers of InO_2^- octahedra interspersed between layers of ZnO (002) with near-perfect periodicity (*15, 16*). Later work found that the superlattice-forming materials could be generalized to $M_2O_3(ZnO)_n$, where *M* is In, Ga, Fe, and other tri-valent metals, or mixtures such as InGa or InFe (*17, 18*). The increased electrical conductivity from n-type doping and decreased thermal conductivity as a result of interface phonon scattering in the superlattices resulted in a zT of 0.1 across a temperature range of 500-900 K for bulk indium zinc oxide (IZO, $In_2O_3(ZnO)_9$) (*19*). Previous work on nanowire thermoelectrics suggests that the phononic contribution to thermal transport can be significantly reduced through size-reduction and surface engineering (*13, 20*). Therefore, the combination of a superlattice structure and a single-crystalline nanowire could lead to a better phonon-scattering and charge-transporting structure, and hence a better thermoelectric material (*21*). In this work, we demonstrate a novel method for the rational design and atomic-level control of nanometer-sized features in the polytypoid $M_2O_3(ZnO)_n$ nanowire system and show both electrical and thermal enhancements in zT for IGZO nanowires as a result of these features.

Synthesis of polytypoid oxide nanowires

IZO and indium gallium zinc oxide (IGZO, $In_{2-x}Ga_xO_3(ZnO)_n$) nanowires can be grown by a chemical vapor transport (CVT) method (*22, 23, 24*). However, it remains difficult to achieve rational control over material properties, such as nanowire diameter and dopant concentration, in addition to maintaining a high yield of superlattice wires. Utilizing a three-step, solid-state diffusion process shown schematically in Fig. 1A, we present a novel method for

producing $M_2O_3(ZnO)_n$ alloy nanowires that allows for a high level of control in manipulating material composition, structure, and properties. As-grown samples of [002]-oriented ZnO nanowire arrays were first coated with mixtures of In, Ga, and Fe using a thermal evaporation system equipped with a quartz crystal monitor. The metal-coated samples were then annealed at 900 °C in oxygen to form arrays of polytypoid alloy nanowires. The superlattice structure remained after further annealing at 900 °C, indicating that the structure is thermally stable. In this work, samples are referred to by the thickness of the metal coating, rather than the chemical formula, due to the natural distribution of nanowire diameter (affecting concentration) and the polytypoid nature of the nanowires. This method has been applied successfully to synthesize nanowires of IZO, IGZO, gallium zinc oxide ($Ga_2O_3(ZnO)_n$), and for the first time, indium iron zinc oxide ($In_{2-x}Fe_xO_3(ZnO)_n$) (Figs. S1 to S4).

Structural analysis

The solid-state diffusion process used to generate the polytypoid $M_2O_3(ZnO)_n$ nanowires maintains the original morphology of the nanowire array and no etching is observed, as seen in the scanning electron microscope (SEM) images taken before (Fig. 1B) and after (Fig. 1C) alloy formation. The $M_2O_3(ZnO)_n$ nanowires made in this study typically have diameters around 80-130 nm and lengths of 10-15 μm, as determined by the dimensions of the starting ZnO nanowires (*25*). The strong 002 peak in the x-ray diffraction (XRD) pattern indicates that the nanowire array maintains a vertical orientation after the conversion (Fig. 1D). No In_2O_3 or Ga_2O_3 peaks were observed in the 10/10 IGZO sample, but the weak unidentified peaks in the 40/40 IGZO sample may belong to an alloy of indium and gallium oxide. In the IGZO nanowire alloys, there is little shift from the position of the ZnO nanowire diffraction peaks, but peak broadening towards smaller angles is observed, suggesting the formation of non-uniform alloys. New peaks

appear in the low-angle region (<10°) for the 40/40 IGZO samples corresponding to spacings of 0.86 and 1.12 nm, which are in good agreement with the predicted lattice constants for $M_2O_3(ZnO)_n$ with n=1 and n=2 (*26*). In addition, we observe higher-order peaks for n=1 and n=2 in the 15-30° range. Energy dispersive X-ray spectrometry (EDS) confirms the presence of In, Ga, and Zn in the IGZO nanowires (Fig. S2), with an In:Ga atomic ratio of approximately 1:1. The relative amounts of In and Ga compared to Zn varies depending on the diameter of the starting ZnO nanowire.

Transmission electron microscope (TEM) images of 10/10 IGZO nanowires (Fig. 2A) show a modulation in contrast along their longitudinal axis, which can be attributed to a superlattice structure. According to previous reports, the superlattice structure consists of planes of InO_2^-octahedra separated by slabs of wurtzite $MZn_nO_{(n+1)}^+$ (M = In, Ga) (*16*). To confirm the structure of our nanowires, Z-contrast scanning transmission electron microscopy (STEM) imaging was done using a 300kV double-Cs-corrected STEM capable of 50 pm resolution. In Z-contrast images, the intensity is approximately proportional to the mean square of the atomic number of the constituent atoms. Thus, using Z-contrast imaging, the position of In (Z = 49) can be unambiguously determined, but Ga (Z = 31) and Zn (Z = 30) cannot be distinguished from one another since their atomic numbers differ by only one. Oxygen cannot be imaged due to its relatively small atomic number. Figure 2B is a Z-contrast image of a 10/10 IGZO nanowire clearly showing the presence of In-enriched layers (brightest lines) oriented perpendicular to the [002] direction. By high-resolution (HR)-STEM it can be seen that the In atoms sit on individual planes and are separated by wurtzite slabs of $MZn_nO_{(n+1)}^+$ of varying thicknesses (Fig. 2C). Only single layers of In atoms are observed in the 10/10 IGZO nanowires, consistent with the layers being composed of octahedrally coordinated InO_2^-, which has been shown to be the most stable

configuration for In within the superlattice structure (*26*). EDS mapping suggests that Ga may also be present in the octahedral layer indicating that the true composition is $In_{1-x}Ga_xO_2^-$ (Fig. S5). In some samples with a high density of inclusions (n = 1, 2), a few double layers can be seen, consistent with early reports by Cannard and Tilley (*27*).

The O atoms on the edges of the MO_2^- octahedral layers are each bonded to three In/Ga atoms and one metal atom within the $MZn_nO_{(n+1)}^+$ layer (*26*). This creates an inversion domain boundary (IDB) in the wurtzite lattice since the Zn-O bonds on either side of the octahedral layer point with the O atoms toward the In/Ga layer (tail-to-tail configuration). The MO_2^- inclusion layer is also associated with a stacking fault, which together with the IDB produces an AaBbAaB**bAc**CaAcCaA (capital and lowercase letters correspond to metal and oxygen atoms, respectively) stacking sequence in which the wurtzite lattice on one side of the In/Ga layer is translated by ⅓<100> (Fig. 2D). The location of the octahedral MO_2^- within the stacking sequence is denoted by the bold **bAc**.

The presence of the IDB at the octahedral layer means that the polarity of the ZnO must revert somewhere within the $MZn_nO_{(n+1)}^+$ slabs to produce the necessary tail-to-tail polarity at the adjacent MO_2^- layer. There are several proposed mechanisms by which the polarity can be reverted (*15, 26, 28, 29*). Yan et al. reported the presence of mirror domain boundaries (MDB) within the ZnO slabs of their IZO films (*15*). However, no such boundaries could be seen in our IGZO nanowires. An additional layer of In atoms within the $MZn_nO_{(n+1)}^+$ slabs may also act as an IDB. The *M* and Zn atoms within the $MZn_nO_{(n+1)}^+$ layer occupy the tetrahedral or trigonal bipyramidal sites within the wurtzite lattice (*16*), and may be ordered in either flat layers or zigzag layers (*26, 29, 30, 31*). Using density functional theory (DFT) calculations Yan et al. and Da Silva et al. compared the relative energies of these two structures and found that the zigzag

modulated structure is more stable for a number of reasons. Firstly, in the zigzag layer, O has an energetically favorable tetrahedral coordination, while in the flat layer O has a coordination of three (*29*). Also, the occupation of the trigonal bipyramidal sites within the wurtzite lattice can cause local lattice distortions and strain within the $MZn_nO_{(n+1)}^+$ slabs. This strain can be reduced by localizing the atoms with trigonal bipyramidal coordination to one boundry. The zigzag layer was found to most effectively reduce this strain (*26, 29*). Zigzags were seen in all four types of alloys synthesized in this study (Figs. S1 to S4), but were not apparent in those alloys with small *n*. Also, since the trigonal bipyramidal sites may be occupied by In, Ga, or Zn atoms in the IGZO nanowires, the zigzags appear faint in the Z-contrast images and in some cases are not discernable. A previous reports observed that zigzags are only present in superlattices with $n > 6$ (*30*). The lattice strain caused by a flat layer of trigonal bipyramidally coordinated In/Ga atoms decreases as the thickness of the $MZn_nO_{(n+1)}^+$ slabs decreases, so the energy difference between the flat and zigzag configurations decreases with decreasing *n* (*26*). Thus, the polarity of the $MZn_nO_{(n+1)}^+$ layers with small *n* may be reversed via a flat layer of trigonal bipyramidal atoms.

In agreement with XRD, the *d* spacings in the $MZn_nO_{(n+1)}^+$ layers are unchanged from (002) in pure ZnO (0.26_2 nm), but the octahedral MO_2^- planes force a local 17% increase in the *d* spacing (0.30_7 nm) on either side of the inclusion layers (Fig. 2E). The *d* spacings were determined by taking an intensity profile across an In/Ga inclusion in a HRSTEM image and measuring the distance between peaks. This change in d-spacing on either side of the In/Ga inclusions corresponds with that reported by Yan et al. and Jie et al. on IZO (*15, 22*). This significant increase in *d* spacings around the inclusion layer is associated with a large amount of lattice strain.

To approximate an n value for the 10/10 IGZO nanowires, the number of atomic layers in each $MZn_nO_{(n+1)}^+$ slab was counted for several nanowires (Fig. 2F). The average n is 11, but the most frequent is 6. n can be related to the spacing (l) between MO_2^- layers by the following equation

$$l\ (\text{nm}) = 0.61_4 + 0.26_2\, n$$

where 0.61_4 nm corresponds to twice the distance of the d spacing immediately adjacent to the MO_2^- octahedral layers and 0.26_2 nm corresponds to the (002) planar spacing within the $MZn_nO_{(n+1)}^+$ slabs. Using this equation the average spacing between MO_2^- octahedral layers in the 10/10 IGZO nanowires 3.50 nm and the most frequent is 2.19 nm.

The amount of metal deposition was varied to determine the relationship between composition and MO_2^- layer density (Fig. 3, A to D). The surface of the 40/40 IGZO nanowire shown in Fig. 3D appears rough due to the presence of oxide particles left over after the solid-state diffusion process. However, most IGZO nanowires in the sample did not show surface particles. Line intensity profiles drawn perpendicular to the MO_2^- inclusions were used to generate power spectra (Fig. 3, E to H) from the nanowires shown in Fig. 3, A to D. The power spectra show the most common frequencies ($1/l$) within the nanowires, providing information regarding the MO_2^- layer spacings and the periodicity of the spacings. As the thickness of metal deposition is increased the most common frequencies shift to higher $1/l$ (smaller l) indicating that the distance between MO_2^- layers decreases with increased metal deposition. The periodicity also increases with metal deposition, which can be seen in the emergence of distinct peaks, such as in Figs. 3G and 3H. The frequencies obtained from the 10/10 power spectrum match the n values that were directly counted in Fig. 2D. As seen in Fig. 3H, the majority of MO_2^- layers in the 40/40 IGZO are separated by 2 or 3 layers of $MZn_nO_{(n+1)}^+$, which is supported

by the low-angle XRD (Fig. 1D) and the HRSTEM image of same 40/40 IGZO nanowire (Fig. S6). It is evident from these power spectra that both *n* and the superlattice periodicity can be controllably tuned by adjusting the amount of metal deposition.

Formation Mechanism

The ability to control the In inclusion density is a direct result of the solid-state diffusion process by which the polytypoid nanowires are produced. The diffusion rates of In, Ga, and Zn within ZnO is extremely high at the 900°C annealing temperature, with values of 6.62×10^{-12}, 1.09×10^{-14}, and 1.13×10^{-12} $cm^2 s^{-1}$, respectively (*32, 33*). DFT calculations show that Zn atoms diffuse through ZnO using Zn vacancies (*34*). Based on their activation energies for diffusion, In and Ga are also thought to diffuse through Zn vacancies, though some controversy exists regarding their true activation energies (*32, 35, 36*). Since In and Ga are substitutional dopants, Zn atoms must diffuse out when the In and Ga atoms diffuse in. The Zn atoms diffuse to the surface of the nanowire, leading to a modulation in the diameter (Fig. S7). In areas of higher inclusion density the diameter of the nanowire is slightly thicker (more In and Ga diffused in, more Zn diffused out) compared to areas of lower inclusion density.

Once the In and Ga diffuse into the nanowire, they strain the wurtzite lattice of the pure ZnO, deforming the structure, and eventually relaxing the strain by creating octahedral In/Ga inclusions and trigonal bipyramidal layers. Defects such as edge dislocations, stacking faults, and IDB are known to attract impurities and can assist in the formation of impurity inclusions (*37*). In some of the nanowires synthesized in this study, especially those made with lower amounts of In and Ga, partial In/Ga inclusions are observed (Fig. 4). The ends of these partial inclusions are usually associated with edge dislocations with the dislocation line lying at the

leading edge of the MO_2^- plane (*38*). Edge dislocations can be seen in Fig. 4 in the HRSTEM image of two partial inclusions. Moiré images taken along the 002 and 102 reflections clearly show the presence of the edge dislocations. Another interesting observation is that the partial inclusions are always connected to one surface of the nanowire (Fig. S7), indicating that the growth of the inclusion starts at the surface and proceeds across the diameter of the nanowire until it either reaches the opposite side or connects with an inclusion growing from the opposite side (Fig. S8).

If the inclusions are growing through a defect-assisted process and the inclusion formation begins at the nanowire surface, then the edge dislocation must somehow nucleate near the surface. One possible scenario is that the edge dislocations are formed on the nanowire surface via heterogeneous nucleation, which occurs with the help of defects such as impurity atoms. Since In has a larger radius compared to Zn, the dissolution of In within the wurtzite lattice will create strain. The presence of dislocations within the lattice can relax some of this strain if the In atoms diffuse towards the dislocations and eventually occupy those lattice positions below the edge dislocations where the lattice is already expanded. The edge dislocation basically creates a "hole" in which the larger In atoms can sit. Due to the high diffusion rate of In within the ZnO lattice the In atoms can rapidly concentrate at the sites of edge dislocations. Since the In atoms have a mutual attraction they will start to crystallize into another phase (octahedrally coordinated MO_2^-), which will flow in one direction towards the dislocation. The growth of the inclusion will continue along the dislocation until the concentration of In within the lattice decreases to the point at which an equilibrium is reached. In the lower concentration samples, more partial inclusions can be observed, likely resulting from insufficient quantities of

In atoms necessary to complete the inclusions. In the 40/40 samples with higher concentrations of In, no partial inclusions were observed.

Electrical Enhancement

The presence of the MO_2^- inclusions alters both the thermal and electrical properties in the converted IGZO nanowires. While ZnO can exhibit relatively high intrinsic electrical conductivity due to formation of oxygen vacancies acting as donor states, the introduction of slight amounts of Al, In, or Ga can further increase the conductivity when substituted for Zn (*39*). The increased electrical conductivity observed at room temperature in the IGZO nanowires when compared to the ZnO nanowires is consistent with that of a slightly doped semiconductor (Fig. 5A). However, considering the relatively large amount of In and Ga incorporation (greater than 2% of metal atoms each from EDS), the observed increase in conductivity is smaller than expected. While the Ga impurities can act as electrical dopants in ZnO when substituted for tetrahedrally coordinated Zn, Ga also sits in the trigonal bipyramidal sites, helping to preserve electroneutrality and reducing the number of generated carriers. Moreover, the MO_2^- inclusions can act as barriers to oxygen diffusion leading to decreased conductivity by suppressing the formation of oxygen vacancies (*40*). However, the linear temperature-dependent resistance of IGZO, as seen in Fig. 5A, is not typical behavior for a slightly doped semiconductor (of which pure ZnO nanowires are an example) or a degenerately doped semiconductor (which should give metallic behavior). This deviation from the classical semiconducting behavior indicates a departure from the typical thermally activated mechanism. The octahedral layers could be acting as potential barriers to electron diffusion, leading to alternative transport mechanisms such as pseudo variable-range hopping or percolation conduction (*41*).

The presence of the inclusion layers also has an effect on the Seebeck voltage (Fig. 5B). At 300 K, the Seebeck coefficient grew in magnitude from –188 μV K^{-1} in ZnO nanowires to –402 μV K^{-1} in IGZO nanowires. This increase may be an effect of the potential barriers, which could act as low-energy electron filters (*42*). When a temperature gradient is applied, charges diffuse to states of lower chemical potential. While most of these states are on the colder side, unoccupied states on the hotter side allow for charge diffusion in the opposing direction, thereby limiting the overall potential that can develop for a given temperature gradient. Charges that participate in back diffusion are referred to as "cold electrons" (for n-type semiconductors) since they posses lower carrier energy. However, potential barriers with appropriate energy levels can act as low energy charge filters by preferentially affecting their mobility (*43*). By limiting the amount of back diffusion, a larger potential can develop, resulting in an increased Seebeck coefficient.

Aside from filtering, the possibility exists that electronic quantum confinement caused by closely spaced inclusion layers contributes to the rise in Seebeck values (*3*). Since l values of less than 2.34 nm (exciton Bohr radius of ZnO) were observed, thermopower enhancement might be due to slight changes in the density of states near the Fermi level (*44*). While difficult to quantify at this time, the random nature of the polytypoid nanowires perhaps plays a role in these and other transport phenomena. Further theoretical and experimental investigations are required in order to paint a clearer picture of this general nanowire system.

Regardless of the source of enhancement, when increases from both the electrical conductivity and the Seebeck coefficient are combined, the resulting power factor ($S^2\sigma$) for the IGZO nanowires is 0.6 mW m^{-1} K^{-2}, which is 58 times larger than that for pure ZnO nanowires

and approximately 6 times greater than the highest reported bulk IZO value at 500 K (Fig. 5C) (*45*).

Carrier mobility enhancement

To ensure that the observed Seebeck enhancement is not due to mere increases in impurity scattering, FET mobilities were measured on the same nanowires from which the electrical conductivity and Seebeck coefficient were determined (Fig. 5D). Both carrier concentration and mobility enhancements were observed when compared to the pure ZnO nanowires. This indicates that the carrier concentration, and not the mobility, is the limiting factor in the electrical conductivity, contrary to what may have been suspected based on the defects that accompany each MO_2^- layer. Furthermore, 177 $cm^2\ V^{-1}\ s^{-1}$ at 300 K is more than twice the field effect mobility value previously measured in single crystalline IGZO thin films (*40*). The nature of the mobility enhancement in the polytypoid IGZO nanowires over IGZO thin films is not fully understood. However, the enhancement over the single crystalline ZnO nanowires may be explained by the induced strain at the MO_2^- layer interfaces. It is well-established that piezoresistive materials, both crystalline and amorphous, demonstrate mobility changes with the application of stress (*46, 47*). As seen in Fig. 2E, the 17% difference in the *d* spacings at the octahedral/wurtzite interface produces a significant amount of strain. Although the inclusions are perpendicular to the transport direction, the mobility could be enhanced by the possible strain-induced changes to the electronic band structure. Further theoretical and experimental work is necessary to determine the extent to which strain plays a role in this polytypoid system.

Thermal conductivity of polytypoid oxide nanowires

Not only do the nanostructured features influence the electronic properties, but they also act as important phonon scattering interfaces, thereby limiting the lattice thermal conductivity (*48*). Compared to literature values for the bulk material, ZnO nanowires demonstrate up to five-fold reduction of thermal conductivity at room temperature (Fig. 6B) (*49*). An estimation of the average phonon mean free path as a function of temperature shows that the limiting factor is the nanowire diameter until the 150–200 K range, where other scattering mechanisms, such as impurity and umklapp scattering, begin to limit the conductivity. As seen in Fig. 6B, the linear segment of the ZnO nanowire plot begins to plateau around that temperature range. The IGZO nanowires, on the other hand, show no such plateau, indicating that the MO_2^- layers are limiting the average phonon mean free path throughout the measured temperature range. At 300 K, IGZO nanowires exhibit a thermal conductivity of 3.3 W m^{-1} K^{-1}, which is only slightly lower than what has been observed for IZO (n=3,4) in the bulk (*50*). However, since bulk IZO has both higher inclusion density and periodicity, it is surprising that the more disordered 5/5 IGZO nanowires exhibit comparable thermal transport properties. While higher inclusion densities are expected to limit the average phonon mean free path, the disordered nature of the polytypoid IGZO structure combined with the nanowire geometry produces similar effects on overall thermal energy propagation.

As a direct result of the enhancements from all three thermoelectric parameters, zT was increased from 1.7×10^{-4} for ZnO nanowires to 0.055 for the IGZO nanowires at 300 K, an enhancement of 2.5 orders of magnitude (Fig. 6C) (*50, 51*). Such zT values represent a factor of ~10 enhancement when compared to the bulk IZO superlattice samples. It is worth noting that

oxide-based thermoelectric modules are typically employed at elevated temperatures (700-1000 K) in actual application, where further power factor enhancements are expected.

Conclusion

In summary, $M_2O_3(ZnO)_n$ (M = In, Ga, Fe) polytypoid nanowires were converted from pure ZnO nanowires using a facile diffusion scheme. This solid-state diffusion process can be used to produce a wide range of ZnO alloys with tunable alloy concentration and inclusion layer density. The inclusion growth is believed to originate from the surface and propagate though the nanowire by a defect-assisted process. Single-nanowire measurements on IGZO show that both the power factor and thermal resistivity were enhanced due to the nanostructured features inherent to this thermally stable system. This is the first experimental demonstration of all three theoretical enhancements of the thermoelectric parameters (S, σ, and k) predicted for modulated nanowire structures. Compared to bulk IZO, IGZO nanowires show a ten-fold improvement in zT at room temperature with further enhancements expected in the range of 500-700 K, which is optimal for ZnO and its alloys. From this study it is apparent that better control of nanometer-scale features could be the key to developing next-generation thermoelectric materials for a more sustainable future.

Acknowledgements

Work at the National Center of Electron Microscopy and Molecular Foundry was supported by the Office of Science, Office of Basic Energy Sciences, of the U.S. Department of Energy under Contract No. DE-AC02—05CH11231.

Acknowledgements: This work was supported by the Director, Office of Science, Office of Basic Energy Sciences, Material Sciences and Engineering Division, of the U.S. Department of Energy under Contract No. DE-AC02-05CH11231. We thank the National Center for Electron Microscopy for the use of their facilities.

References

1. A. I. Hochbaum, P. Yang, *Chem. Rev.*, (2009).
2. G. J. Snyder, E. S. Toberer, *Nature Materials* **7**, 105 (Feb, 2008).
3. L. D. Hicks, M. S. Dresselhaus, *Phys. Rev. B* **47**, 16631 (1993).
4. D. Donadio, G. Galli, *Phys. Rev. Lett.* **102**, 4 (May, 2009).
5. J. H. Lee, G. A. Galli, J. C. Grossman, *Nano Lett.* **8**, 3750 (Nov, 2008).
6. P. Martin, Z. Aksamija, E. Pop, U. Ravaioli, *Phys. Rev. Lett.* **102**, 125503 (2009).
7. T. C. Harman, P. J. Taylor, M. P. Walsh, B. E. LaForge, *Science* **297**, 2229 (Sep, 2002).
8. A. I. Boukai *et al.*, *Nature* **451**, 168 (Jan, 2008).
9. B. Poudel *et al.*, *Science* **320**, 634 (May, 2008).
10. J. P. Heremans *et al.*, *Science* **321**, 554 (Jul, 2008).
11. H. Bottner, G. Chen, R. Venkatasubramanian, *MRS Bull.* **31**, 211 (Mar, 2006).
12. K. F. Hsu *et al.*, *Science* **303**, 818 (Feb, 2004).
13. A. I. Hochbaum *et al.*, *Nature* **451**, 163 (Jan 10, 2008).
14. C.-Y. Wen *et al.*, *Science* **326**, 1247 (Jan 1, 2009).
15. Y. Yan *et al.*, *Appl. Phys. Lett.* **73**, 2585 (Nov 2, 1998).
16. N. Kimizuka, M. Isobe, M. Nakamura, *J. Solid State Chem.* **116**, 170 (Apr, 1995).
17. T. Horlin, G. Svensson, E. Olsson, *J. Mater. Chem.* **8**, 2465 (Nov, 1998).
18. C. F. Li, Y. Bando, M. Nakamura, N. Kimizuka, *J. Solid State Chem.* **142**, 174 (Jan, 1999).
19. H. Ohta, W. S. Seo, K. Koumoto, *J. Am. Ceram. Soc.* **79**, 2193 (Aug, 1996).
20. D. Li, Y. Wu, R. Fan, P. Yang, A. Majumdar, *Appl. Phys. Lett.* **83**, 3186 (2003).
21. Y. Lin, M. Dresselhaus, *Phys. Rev. B* **68**, 075304 (Jan 1, 2003).
22. J. S. Jie, G. Z. Wang, X. H. Han, J. G. Hou, *J. Phys. Chem. B* **108**, 17027 (Nov 4, 2004).
23. C. W. Na, S. Y. Bae, J. Park, *J. Phys. Chem. B* **109**, 12785 (Jul 7, 2005).
24. D. P. Li, G. Z. Wang, Q. H. Yang, X. Xie, *J Phys Chem C* **113**, 21512 (2009).
25. M. H. Huang *et al.*, *Science* **292**, 1897 (Jun 8, 2001).
26. J. L. F. Da Silva, Y. F. Yan, S. H. Wei, *Phys. Rev. Lett.* **100**, 255501 (Jun 27, 2008).
27. P. J. Cannard, R. J. D. Tilley, *J. Solid State Chem.* **73**, 418 (Apr, 1988).
28. Y. Ding, X. Y. Kong, Z. L. Wang, *Phys. Rev. B* **70**, 235408 (2004).
29. Y. Yan, J. L. F. Da Silva, S.-H. Wei, M. Al-Jassim, *Appl. Phys. Lett.* **90**, 261904 (2007).
30. C. Li, Y. Bando, M. Nakamura, N. Kimizuka, *J. Electron Microsc.* **46**, 119 (1997).
31. M. Isobe, N. Kimizuka, M. Nakamura, T. Mohri, *Acta Crystallographica Section C* **50**, 332 (1994).
32. D. G. Thomas, *J. Phys. Chem. Solids* **9**, 31 (1959).
33. I. Broser *et al.*, *Physics of II-VI and I-VII Compounds, Semimagnetic Semiconductors*. Landolt-Börnstein: Numerical Data and Functional Relationships in Science and Technology (Springer-Verlag, New York, 1982), vol. 17.
34. P. Erhart, K. Albe, *Appl. Phys. Lett.* **88**, 201918 (2006).
35. T. Nakagawa *et al.*, *Jpn. J. Appl. Phys.* **47**, 7848 (2008).
36. T. Nakagawa *et al.*, *Jpn. J. Appl. Phys.* **46**, 4099 (2007).
37. G. Popovici *et al.*, *Appl. Phys. Lett.* **71**, 3385 (1997).
38. C. Li, Y. Bando, M. Nakamura, N. Kimizuka, *Micron* **31**, 543 (2000).
39. G.-D. Yuan *et al.*, *Adv. Mater.* **20**, 168 (2008).

40. K. Nomura *et al.*, *Science* **300**, 1269 (2003).
41. K. Nomura *et al.*, *Appl. Phys. Lett.* **85**, 1993 (2004).
42. A. Shakouri, E. Lee, D. Smith, V. Narayanamurti, J. Bowers, *Microscale Therm Eng* **2**, 37 (Jan 1, 1998).
43. L. W. Whitlow, T. Hirano, *J. Appl. Phys.* **78**, 5460 (1995).
44. R. Senger, K. Bajaj, *Phys. Rev. B* **68**, 045313 (Jan 1, 2003).
45. O. Malochkin, W. S. Se, K. Koumoto, *Jpn. J. Appl. Phys., Part 2* **43**, L194 (2004).
46. H. Gleskova *et al.*, *J. Non-Cryst. Solids* **338-340**, 732 (2004).
47. Z. Alahmed, H. Fu, *Phys. Rev. B* **77**, (2008).
48. G. Chen, A. Narayanaswamy, C. Dames, *Superlattice Microst* **35**, 161 (Jan 1, 2004).
49. U. Ozgur *et al.*, *J Electron Mater* **35**, 550 (Jan 1, 2006).
50. H. Kaga, R. Asahi, T. Tani, *Jpn J Appl Phys 1* **43**, 7133 (Jan 1, 2004).
51. L. Fang *et al.*, *J Supercond Nov Magn* **23**, 889 (Aug 30, 2010).

Figure Captions

Fig. 1. (**A**) Schematic illustration of the synthetic method. (**B** and **C**) Scanning electron microscope images of arrays of the as-grown ZnO nanowires (B) and IGZO nanowires prepared with 5/5 nm In/Ga deposition (C). (**D**) XRD patterns of ZnO nanowires (bottom) and IGZO nanowires prepared with 10/10 (middle) and 40/40 nm (top) of In and Ga metals using Cu k_α irradiation. Longer acquisition times were used below 12° for better signal to noise and thus were normalized separately from the rest of the pattern.

Fig. 2. (**A**) TEM image of multiple IGZO nanowires. (**B**) Z-contrast STEM image of a 10/10 IGZO nanowire. The Z contrast in the image clearly shows that In atoms are preferentially located within layers oriented perpendicularly to the nanowire growth direction. (**C**) HRSTEM image of an IGZO nanowire showing individual MO_2^- layers sandwiched between multiple $MZn_nO_{(n+1)}^+$ layers. (**D**) HRSTEM image highlighting the change in stacking sequence across a MO_2^- layer. (**E**) Intensity line profile and *d* spacing across a MO_2^- layer taken from a HRSTEM image. On either side of the inclusion, the *d* spacing shows an expansion of ~17% relative to that of pure ZnO. (**F**) Frequency of different *n* values of the $MZn_nO_{(n+1)}^+$ layers measured from HRSTEM images of several 10/10 IGZO nanowires. The average *n* is 11 and the most frequent is 6.

Fig. 3. (**A** to **D**) Z-contrast STEM images of IGZO nanowires prepared with 10, 20, 40, and 80 nm of metal (1:1 In:Ga by film thickness), respectively. (**E** to **H**) Power spectra generated using line intensity profiles drawn along the length of the nanowires showing the frequency of reciprocal distance between MO_2^- layers for (**A** to **D**). The distance between MO_2^- layers decreases with increasing thickness of metal deposition. The periodicity of the MO_2^- layer spacings also improves.

Fig. 4. (**A**) HRSTEM image of IGZO oriented on the [010] zone axis with two incomplete MO_2^- layers and the corresponding FFT (inset). (**B** and **C**) Moiré images of the 002 (B) and 102 (C) reflections clearly showing the presence of edge dislocations at the end of each incomplete MO_2^- layer.

Fig. 5. (**A**) Electrical conductivity as a function of temperature for a 120-nm diameter 5/5 IGZO nanowire (blue circles) and a 110-nm diameter ZnO nanowire (red squares). (**B** and **C**) Seebeck coefficient (B) and power factor (C) as a function of temperature measured for the same nanowires in (A). Inset shows a SEM of an individual nanowire in a four-point FET/Seebeck device. (**D**) Carrier concentration as a function of mobility, as measured from the FET geometry. No diameter dependence was observed for ZnO or IGZO nanowires in the range of 75–130 nm.

Fig. 6. (**A**) SEM of an individual IGZO nanowire bridging two suspended membranes on a prefabricated MEMS device used for thermal conductivity measurements. (**B**) Thermal conductivity as a function of temperature for both a 120-nm 5/5 IGZO nanowire and a 90-nm ZnO nanowire. (**C**) Figure of merit, zT, of IGZO nanowires compared with ZnO nanowires showing an enhancement of 2.5 orders of magnitude after alloying.

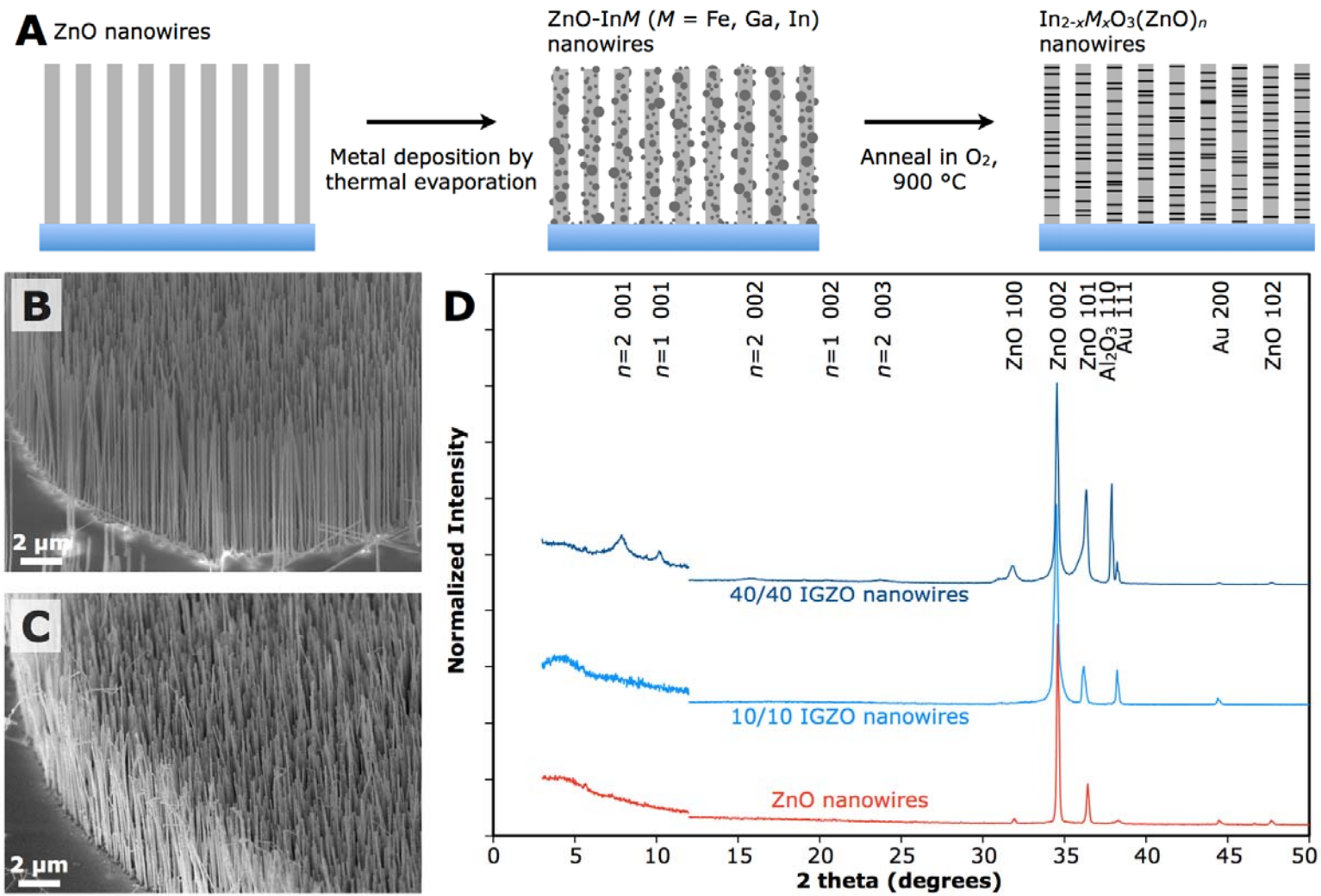
A
ZnO nanowires
Metal deposition by thermal evaporation
ZnO-InM (M = Fe, Ga, In) nanowires
Anneal in O2, 900 °C
In2-xMxO3(ZnO)n nanowires
B
2 µm
C
2 µm
D
n=2 001
n=1 001
n=2 002
n=1 002
n=2 003
ZnO 100
ZnO 002
ZnO 101
Al2O3 110
Au 111
Au 200
ZnO 102
40/40 IGZO nanowires
10/10 IGZO nanowires
ZnO nanowires
Normalized Intensity
0
5
10
15
20
25
30
35
40
45
50
2 theta (degrees)

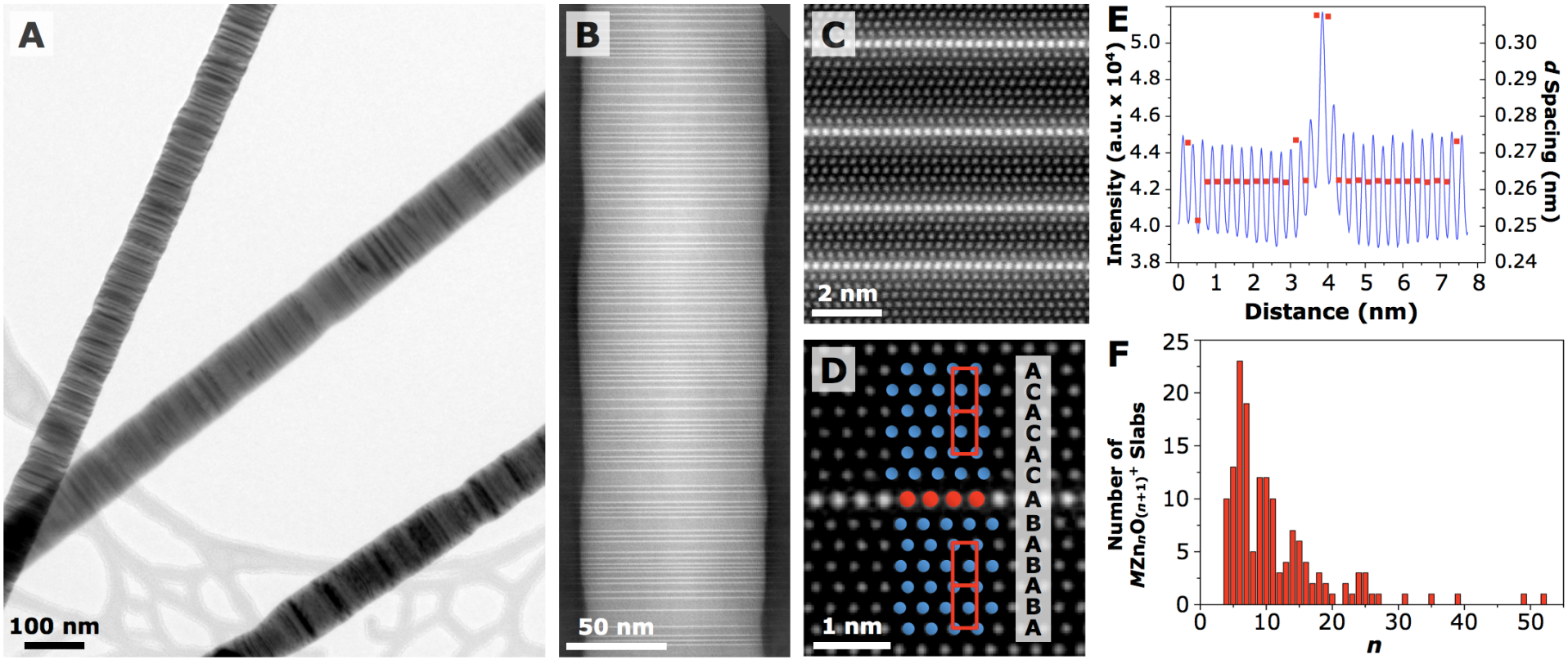
A
100 nm
B
50 nm
C
2 nm
D
1 nm
ACACACABABABA
E
Intensity (a.u. x 10^4)
d Spacing (nm)
Distance (nm)
F
Number of MZn_nO_(n+1)^+ Slabs
n

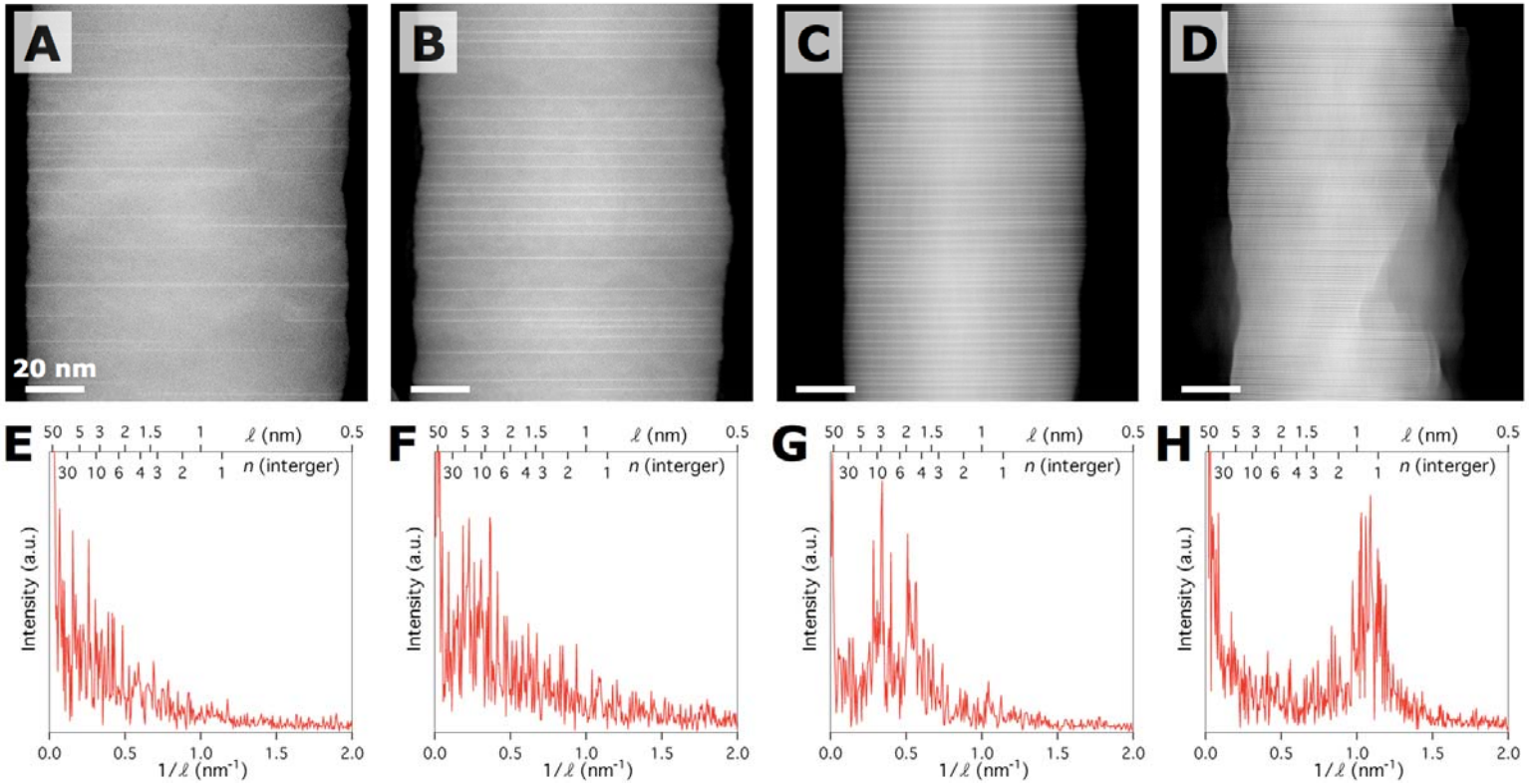
A
B
C
D
20 nm
E
F
G
H
ℓ (nm)
n (interger)
Intensity (a.u.)
1/ℓ (nm⁻¹)

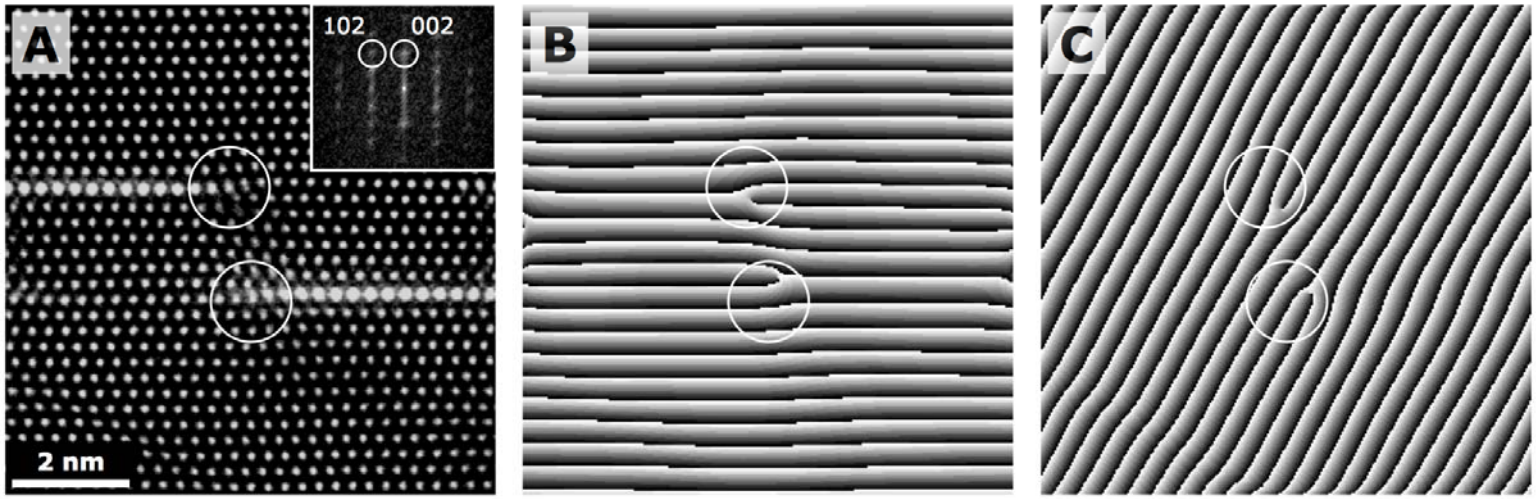
A
102
002
2 nm
B
C

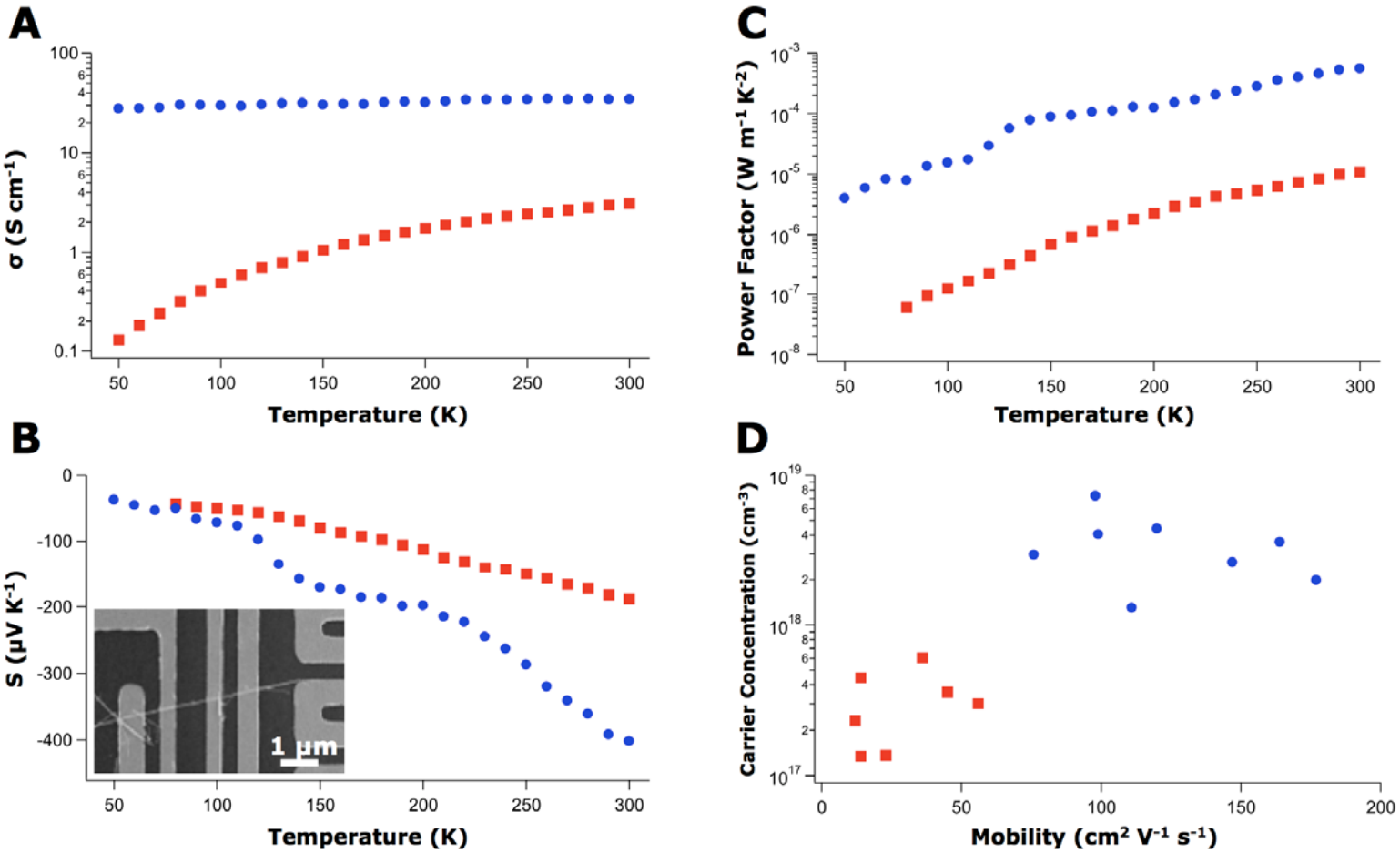
A
σ (S cm-1)
Temperature (K)
B
S (μV K-1)
1 μm
Temperature (K)
C
Power Factor (W m-1 K-2)
Temperature (K)
D
Carrier Concentration (cm-3)
Mobility (cm2 V-1 s-1)

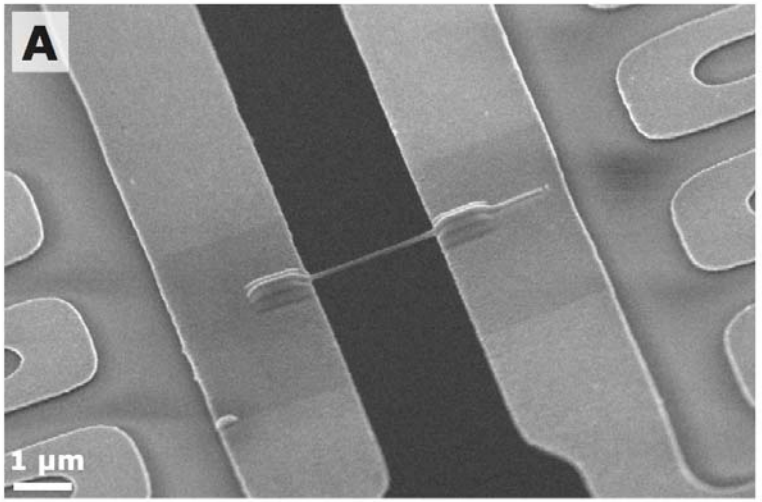
A
1 µm

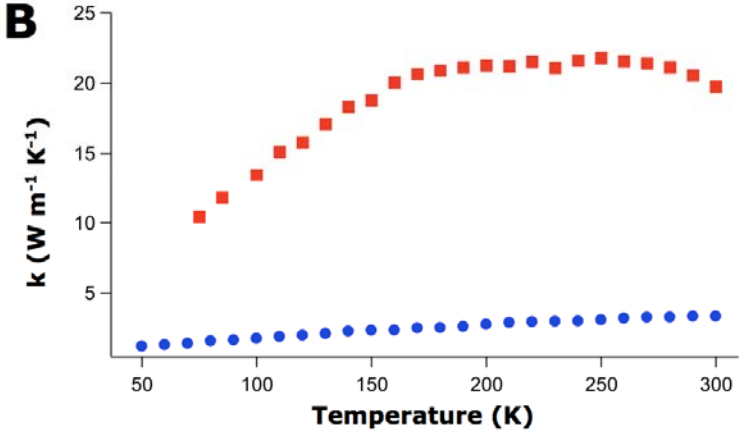
B
k (W m-1 K-1)
25
20
15
10
5
50
100
150
200
250
300
Temperature (K)

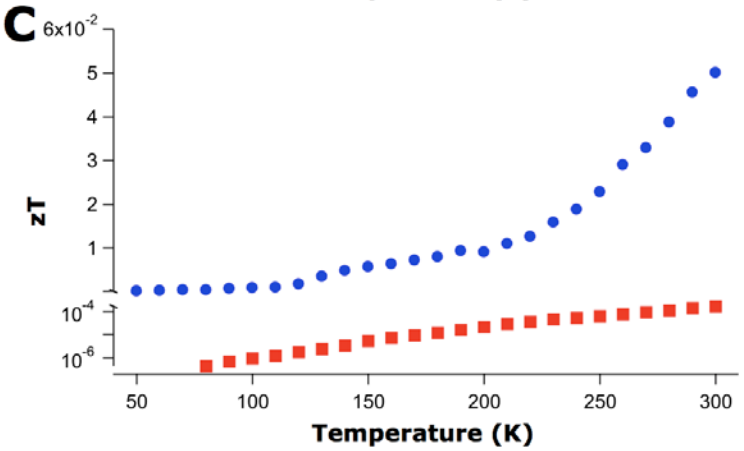
C
zT
6x10-2
5
4
3
2
1
10-4
10-6
50
100
150
200
250
300
Temperature (K)